



PERGAMON

Available online at www.sciencedirect.com

SCIENCE @ DIRECT®

International Journal of
**Multiphase
Flow**

International Journal of Multiphase Flow 29 (2003) 771–794

www.elsevier.com/locate/ijmulflow

Numerical simulation of a fuel droplet laden exothermic reacting mixing layer

Vikas C. Khatumria, Richard S. Miller *

Department of Mechanical Engineering, Clemson University, Clemson, SC 29634-0921, USA

Received 19 September 2002; received in revised form 19 February 2003

Abstract

Numerical simulations are conducted of two-dimensional exothermic reacting mixing layers laden with liquid fuel droplets. An irreversible reaction of the form $Fuel + rOxidizer \rightarrow (1 + r)Products + Heat$ with Arrhenius kinetics is considered where the fuel species consists of both a gaseous fuel stream and liquid fuel droplets. A variety of configurations are simulated including cases for which the droplet species and/or the carrier fuel is either reacting or non-reacting. The droplets are tracked individually in the Lagrangian reference frame while the compressible form of the Navier–Stokes equations together with transport equations for all species govern the gas phase. The simulation parameters study the effects of the fuel composition, reaction stoichiometry, mass loading ratio, droplet Stokes number and the flow forcing amplitude. The simulations reveal that non-reacting carrier fuel configurations fail to achieve robust combustion, suggesting the primary role of carrier gas fuel to the reaction. Local flame extinction is markedly increased for non-reacting fuel droplets due to latent heat effects. In contrast, liquid droplets which contribute fuel to the reaction overcome the associated latent heat effects and show a relatively robust reaction with minimal local extinction.

© 2003 Elsevier Science Ltd. All rights reserved.

Keywords: Two-phase; Turbulence; Droplets; Mixing layer; Two-way coupled; Numerical simulation; Reacting flow

1. Introduction

Due to the large occurrence in a variety of natural and practical applications, multiphase turbulent combustion has attracted significant engineering interest. These applications include liquid fueled combustors, liquid fuel injected combustion engines, solid propellant combustion and fire

* Corresponding author. Tel.: +1-864-656-6248.

E-mail address: rm@clemson.edu (R.S. Miller).

suppression and control. All of these situations involve a dispersed phase species which considerably affects the thermochemical nature of the surrounding carrier gas flow. Fuel droplets and solid particle propellants are two examples of important dispersed phase species in combustion. The evaporation of fuel droplets largely determines the distribution of the combustible gaseous fuel/air mixture. Therefore, mixing and evaporation processes in liquid fuel spray combustors have marked effects on ignition characteristics. These situations involve a large number of discrete fuel droplets convecting and vaporizing in a continuous gas phase species, and their mathematical description involves complex non-linear couplings of momentum, energy and mass exchange.

The present effort is a numerical investigation of gaseous non-premixed turbulent flames laden with reacting discrete liquid fuel droplets. The “Eulerian–Lagrangian” approach is adopted wherein every individual particle or droplet is tracked in a time accurate manner in a Lagrangian reference frame, whereas the gas phase flow variables are solved in the traditional Eulerian reference frame. We restrict the discussion to cases for which the dispersed phase: (1) has a relatively small and negligible volume fraction, (2) is composed of discrete, non-connected and approximately spherical droplets, (3) has negligible effects due to droplet collisions, breakup and coalescence and (4) chemical reactions are assumed to result in “cluster burning” in the gas phase; not in isolated flames surrounding individual droplets.

Significant insight has been gained into the evolution of both homogeneous and non-homogeneous particle-laden turbulent flows based on early experimental, theoretical and computational methods. In particular, the mixing layer formed by the merging of parallel flowing fluid streams remains one of the classic flow geometries for fundamental studies of turbulent mixing and combustion. These turbulent shear flows are characterized by large scale organized vortical structures which substantially affect the dispersed phase dynamics. Early investigations into the evolution of mixing layers show that the large scale stream and spanwise vortical structures (Winant and Browand, 1974; Brown and Roshko, 1974) play a dominant role in the development of the layer and its transition to turbulence (Huang and Ho, 1990; Moser and Rogers, 1991). Experimental measurements of particle dispersion in non-homogeneous free shear layers have shown that the particle concentration field is well correlated with the large scale vortical structures in these flows (Lazaro and Lasheras, 1989). Chein and Chung (1987) studied the effects of vortex pairing on solid particle dispersion in a planar shear layer.

It is well understood that solid particles tend to be centrifuged away from the high vorticity regions and migrate into high strain regions of the mixing layer (Squires and Eaton, 1991). This phenomena is referred to as “preferential concentration” and has been observed for a wide variety of flow configurations (Eaton and Fessler, 1994). The extent to which preferential concentration occurs depends primarily on the Stokes number (ratio of particle time constant to eddy turnover time scale). It has been observed that the particle dispersion is maximized for “intermediate” Stokes numbers near unity. Very small particles ($St \ll 1$) closely follow fluid motions and behave essentially as fluid elements, whereas large particles ($St \gg 1$) are predominantly unaffected by the flow owing to inertial dominance (Wen et al., 1992; Martin and Meiburg, 1994; Elghobashi, 1994).

Solid particle flows can be described as either “one-way” coupled, when the dispersed phase mass loading is small and the flow remains essentially unaltered by the particles, or as “two-way” coupled when the loading is increased to the point at which the particles modulate the flow primarily through integrated particle drag effects (Elghobashi and Truesdell, 1993). The majority of previous investigations have concentrated on one-way coupled flows owing to the combined

numerical difficulties of calculating the phase coupling terms and tracking sufficiently large number of particles in two-way coupled flows. Exceptions include Meiburg et al. (2000) who numerically investigated the solid particle-laden mixing layer finding strongest two-way coupling effects for intermediate Stokes numbers. The majority of simulations for two-way coupled solid particle flows have been performed for homogeneous turbulence (Boivin et al., 1998; Squires and Eaton, 1990; Elghobashi and Truesdell, 1993; Squires and Eaton, 1994; Truesdell and Elghobashi, 1994; Maxey et al., 1997; Sundaram and Collins, 1999).

In addition to the drag force which predominantly governs phase coupling in solid particle flows, turbulence modulation in evaporating droplet flows is also governed by both mass and thermal energy exchange between the gas and liquid phases. Furthermore, the droplet time constant is a function of both time and space. This may significantly alter the overall preferential concentration and turbulence modulation for evaporating droplets relative to the analogous effects observed for solid particles. Mashayek (1998a,b) conducted simulations of both isotropic and homogeneous shear box turbulence with two-way coupled liquid droplets. Miller and Bellan (1998, 1999, 2000) extended two-way coupled simulations to non-homogeneous flows simulating a three-dimensional (3D) planar mixing layer having one stream laden with evaporating hydrocarbon droplets. Their study shows that the droplet laden stream reaches a state of saturation due to the combined effects of gas cooling and growth of the evaporated vapor mass fraction. However, the evaporation of the droplets inside the mixing layer proceeds to completion because of the presence of the higher temperature, low vapor content, fluid from the non-laden stream.

The above mentioned citations have only studied non-reacting flows. The extent of research on reacting two-phase flows is more limited, and has typically been focussed on experimental studies. Wakabayashi et al. (1998) observed the detailed structure of a laminar spray flame in two-dimensional (2D) counterflow configuration using particle tracking velocimetry to observe the Lagrangian behavior of evaporating and combusting droplets across the spray flame. An experimental system was designed by Karpetsis and Gomez (2000) recently for the study of well defined turbulent non-premixed spray flames using a variety of complementary diagnostic techniques including phase Doppler interferometric techniques and Raman spectroscopy. In contrast, simulations of two-phase reacting flows have received considerably less attention. Miller and Bellan (1998) investigated an infinitely fast adiabatic reaction based on a passive conserved scalar mixture fraction in the context of analyzing the validity of the assumed PDF method for two-phase combustion. Smith et al. (1998) proposed a conditional moment closure model for reacting particles in turbulent non-premixed combustion using a pseudo-spectral solution technique for forced isotropic turbulent flow to validate the model. Mashayek (2000) extended their earlier simulations to simulate reacting homogeneous shear turbulence. In this case, fuel droplets are immersed in a carrier gas oxidizer and a simple chemical reaction of the form $Fuel + Oxidizer \rightarrow Products$ was employed. Miller (2001) recently investigated the effects of non-reacting solid particle and liquid droplet loading on an exothermic reacting mixing layer. Both streams were laden with either particles or droplets and a simple chemical reaction of the form $Fuel + rOxidizer \rightarrow (1 + r)Products$ was considered. Results from these studies illustrate the effects of the mass loading ratio, the initial droplet time constant, and several thermodynamic droplet parameters on the turbulence evolution.

The primary objective of the present investigation is to conduct numerical simulations to investigate the complex couplings of turbulent flames with a reacting dispersed phase in the form of

evaporating fuel droplets in a turbulent combusting environment. The effects of liquid/gas fuel composition, flow forcing, dispersed phase mass loading, droplet size, and the reaction stoichiometric coefficient are considered. Following the approach of Miller (2001) a 2D temporally developing mixing layer is considered as a model flow representative of turbulent reacting flows due to the unrealistically large computer resources that would be required to capture transition to turbulence in a 3D reacting two-phase mixing layer. Although vortex stretching is not present in the 2D model flows, the qualitative effects of droplet interactions with a highly convoluted flame front, droplet evaporation, preferential concentration, local flame extinction, and vortex pairing, remain intact in the 2D simulations, and the assumption is therefore not considered to significantly impact the results or their interpretation. The paper is organized as follows: The formulation and mixing layer configuration are described in Section 2. The computational approach and flow parameters are the topic of discussion of Section 3. Results from the simulations are presented in Section 4, which includes subsections addressing flow visualization, effects of fuel composition, the dispersed phase mass loading ratio, the initial Stokes number, the stoichiometric coefficient and the forcing amplitude. Conclusions are provided in Section 5.

2. Formulation

The Lagrangian transport of evaporating droplets through a continuous, calorically perfect and chemically reacting carrier gas flow is characterized by the following governing equations. The two-phase flow formulation has been presented previously, and will therefore only be summarized here: The reader may refer to Miller and Bellan (1999) and Miller (2001) for additional details. All flows considered for the present investigation are two-dimensional (2D). The subscripts F, O, P and V refer to the gaseous fuel, oxidizer, product and evaporated vapor species, respectively. Subscript G refers to the multispecies gas phase mixture, and subscript L denotes the liquid (droplet) phase. The compressible form of the governing equations for the gas phase are:

$$\frac{\partial \rho}{\partial t} + \frac{\partial}{\partial x_j} [\rho u_j] = S_I, \quad (1)$$

$$\frac{\partial}{\partial t} (\rho u_i) + \frac{\partial}{\partial x_j} [\rho u_i u_j + P \delta_{ij} - \tau_{ij}] = S_{II,i}, \quad (2)$$

$$\frac{\partial}{\partial t} (\rho e_t) + \frac{\partial}{\partial x_j} \left[(\rho e_t + P) u_j - \lambda \frac{\partial T}{\partial x_j} - u_i \tau_{ij} \right] = S_{III} - \dot{\omega}_P \Delta H^0, \quad (3)$$

$$P = \rho \sum_{\alpha} [R^0 / W_{\alpha}] T, \quad (4)$$

where ρ is the gas phase density, u_i , is the gas phase velocity, P is the thermodynamic pressure, $e_t = e + u_i u_i / 2$ is the total gas energy where e is the internal energy, the universal gas constant is R^0 , μ is the viscosity, and λ is the thermal conductivity. The right-hand side terms, S_I , $S_{II,i}$ and S_{III} describe the phase couplings of mass, momentum and energy, respectively, and are discussed below. All gaseous species are assumed to obey the ideal gas law (Eq. (4)) over the range of thermodynamic conditions investigated.

An irreversible and exothermic reaction of the form $Fuel + rOxidizer \rightarrow (1 + r)Products$ is considered through the solution of transport equations for the mass fractions (Y_γ) of the oxidizer ($\gamma = O$), fuel ($\gamma = F$), product ($\gamma = P$), and evaporated vapor ($\gamma = V$):

$$\frac{\partial}{\partial t}(\rho Y_\gamma) + \frac{\partial}{\partial x_j} \left[\rho Y_\gamma u_j - \rho \Gamma \frac{\partial Y_\gamma}{\partial x_j} \right] = \dot{\omega}_\gamma + S_{L,\gamma}, \quad (5)$$

where Γ is the Fickian species diffusion coefficient. Note that separate transport equations are solved for the original carrier gas fuel and evaporated fuel vapor allowing for the distinction of fuel originating from droplets. The phase coupling term $S_{L,\gamma}$ is discussed below. The chemical kinetics are based on the Arrhenius form of the reaction rate ($\dot{\omega}_\gamma$):

$$\dot{\omega}_O = -r\rho K_R(T) \left(\frac{W_P}{W_F} \right) Y_O Y_F, \quad (6)$$

$$\dot{\omega}_F = -\rho K_R(T) \left(\frac{W_P}{W_O} \right) Y_O Y_F, \quad (7)$$

$$\dot{\omega}_P = +(1 + r)\rho K_R(T) \left(\frac{W_P}{W_F} \right) \left(\frac{W_P}{W_O} \right) Y_O Y_F, \quad (8)$$

with temperature dependent reaction coefficient: $K_R(T) = A^0 \exp[-E^0/(R^0 T)]$, where E^0 is the activation energy, A^0 is the reaction rate constant, and W_γ is the molecular weight of species γ .

Based on the findings of Miller et al. (1998), the droplet evolution is assumed to obey a variant of the classical “ D^2 law”. The transient position (X_i), velocity (v_i), temperature (T_d) and mass (m_d) of a single droplet are described by the modeled Lagrangian equations as:

$$\frac{dX_i}{dt} = v_i, \quad (9)$$

$$\frac{dv_i}{dt} = \frac{F_i}{m_d}; \quad \text{with } F_i = m_d \left(\frac{f_1}{\tau_d} \right) (u_i - v_i), \quad (10)$$

$$\frac{dT_d}{dt} = \frac{Q + \dot{m}_d L_V}{m_d C_L}; \quad \text{with } Q = m_d \left(\frac{f_2}{\tau_d} \right) \left(\frac{Nu C_{p,G}}{3 Pr_G} \right) (T - T_d), \quad (11)$$

$$\frac{dm_d}{dt} = \dot{m}_d = -m_d \left(\frac{1}{\tau_d} \right) \left(\frac{Sh}{3 Sc_G} \right) \ln[1 + B_M], \quad (12)$$

where F_i is the modified Stokes drag force, Q is the heat flux to the surroundings, the subscript d denotes individual droplet conditions, the droplet time constant for Stokes flow is $\tau_d = \rho_L D^2 / (18\mu)$, D is the droplet diameter, C_L is the heat capacity of the liquid, and the latent heat of evaporation is L_V . A mass averaging is used to calculate the gas mixture heat capacity; $C_{p,G} = \sum_\alpha Y_\alpha C_{p,\alpha}$ (evaluated at droplet locations). For the gas phase, the Prandtl and Schmidt numbers are $Pr_G = \mu C_{p,G} / \lambda$ and $Sc_G = \mu / (\rho \Gamma)$, respectively. The Nusselt (Nu) and Sherwood (Sh) numbers are modified for finite Reynolds number effects based on the semi-empirical Ranz–Marshall correlations:

$$Nu = 2 + 0.552 Re_d^{1/2} Pr_G^{1/3}, \quad Sh = 2 + 0.552 Re_d^{1/2} Sc_G^{1/3}. \quad (13)$$

The evaporation rate is driven by the mass transfer number; $B_M = (Y_{sf} - Y_V)/(1 - Y_{sf})$ (subscript sf denotes droplet surface conditions). The Stokes drag is empirically corrected for finite droplet Reynolds numbers and evaporation (Miller et al., 1998) through f_1 defined as:

$$f_1 = \frac{1 + 0.0545 Re_d + 0.1 Re_d^{1/2} (1 - 0.03 Re_d)}{1 + a |Re_b|^b}, \quad (14)$$

$$a = 0.09 + 0.077 \exp(-0.4 Re_d), \quad b = 0.4 + 0.77 \exp(-0.04 Re_d), \quad (15)$$

where $Re_d = \rho_G u_s D / \mu_G$ is related to the slip velocity, and $Re_b = \rho_G u_b D / \mu_G$ is related to the blowing velocity. $u_s = |u_i - v_i|$ is the slip velocity magnitude, and u_b is obtained from the relation $\dot{m}_d = \pi \rho_G D^2 u_b$.

The function $f_2 = \beta / (e^\beta - 1)$ is an analytical evaporative heat transfer correction, where the non-dimensional evaporation parameter, $\beta = -1.5 Pr_G \tau_d \dot{m}_d / m_d$, is constant for droplets obeying the “ D^2 law.” The vapor surface mass fraction is calculated directly from the surface molar fraction (χ_{sf}) which is obtained by equating the vapor and liquid fugacities at the surface (i.e. $\chi_{sf} P = P_{sat}$), where the Clausius–Clapeyron relation provides the saturation pressure (P_{sat}) as:

$$Y_{sf} = \frac{\chi_{sf}}{\chi_{sf} + (1 - \chi_{sf}) W_G / W_V}, \quad \chi_{sf} = \frac{P_{atm}}{P} \exp \left\{ \frac{L_V}{R_V} \left(\frac{1}{T_{B,L}} - \frac{1}{T_d} \right) \right\}, \quad (16)$$

where P_{atm} is standard atmospheric pressure, $T_{B,L}$ is the saturation temperature at P_{atm} (i.e. the normal boiling temperature) and the latent heat is a linear function of temperature for calorically perfect species: $L_V = h_V^0 - (C_L - C_{p,V}) T_d$ where h_V^0 is the vapor reference enthalpy.

The above formulation leads to the phase coupling terms expressed as:

$$S_I = - \sum_{\alpha} \left\{ \frac{w_{\alpha}}{\Delta x_1 \Delta x_2 \Delta x'_3} [\dot{m}_d]_{\alpha} \right\}, \quad (17)$$

$$S_{II,i} = - \sum_{\alpha} \left\{ \frac{w_{\alpha}}{\Delta x_1 \Delta x_2 \Delta x'_3} [F_i + \dot{m}_d v_i]_{\alpha} \right\}, \quad (18)$$

$$S_{III} = - \sum_{\alpha} \left\{ \frac{w_{\alpha}}{\Delta x_1 \Delta x_2 \Delta x'_3} \left[v_i F_i + Q + \dot{m}_d \left\{ \frac{v_i v_i}{2} + h_{V,sf} \right\} \right]_{\alpha} \right\}, \quad (19)$$

where the summations are over local individual droplet contributions, $h_{V,sf} = C_{p,V} T_d + h_V^0$ is the evaporated vapor enthalpy at the droplet surface, and the single droplet evaporation rate (\dot{m}_d), drag force (F_i) and heat transfer rate (Q) are specified by Eqs. (10)–(12). The local summations are over all droplets residing within a local numerical discretization element ($\Delta x_1 \Delta x_2$; for 2D). A geometrical weighting factor, w_{α} , is employed to distribute the individual droplet contributions to the four nearest neighbor surrounding grid points. A characteristic length in the hypothetical x_3 direction ($\Delta x'_3$) is specified to define the source terms on a per unit volume basis since the droplets are modeled as spherical entities and not as cross sections of infinitely long cylinders (see below). A conservative operator is further used to minimally smooth the source terms to retain numerical stability of the Eulerian gas phase equations (Miller and Bellan, 1999). In addition, the 2D simulations allow for a relatively very fine grid resolution aimed at keeping even the smoothed source fields local to the originating droplets.

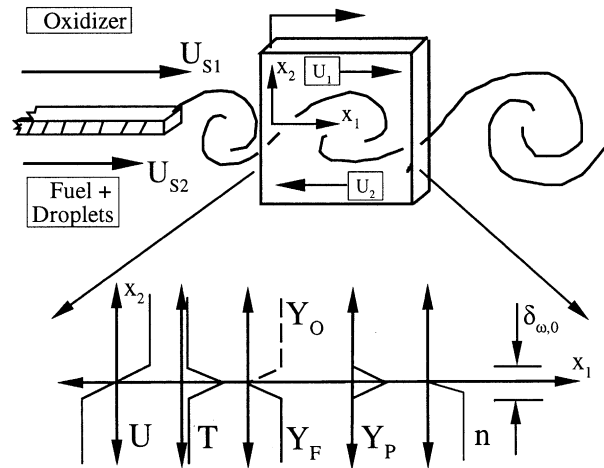


Fig. 1. Schematic of the two-phase temporally developing mixing layer configuration.

2.1. Temporally developing mixing layer configuration

The flow configuration considered is that of a 2D temporally developing mixing layer. Fig. 1 shows a schematic of the simulation domain used in the present investigation. The streamwise (x_1) and cross stream (x_2) domain lengths are L_1 and L_2 , respectively. Stream 1 ($x_2 > 0$) is composed of pure oxidizer, whereas Stream 2 ($x_2 < 0$) is pure fuel. Stream 2 is uniformly laden with droplets for all two-phase simulations. The initial vorticity thickness is $\delta_{\omega,0}$, where $\delta_{\omega}(t) = \Delta U_0 \langle \partial u_1 / \partial x_2 \rangle_{\max}$; the brackets $\langle \rangle$ indicate averaging over the homogeneous x_1 direction and the mean velocity difference across the layer, $\Delta U_0 = U_1 - U_2$, is calculated from a specified value of the convective Mach number (M_c) (Papamoschou and Roshko, 1988).

The base flow mean velocity, mass fraction, temperature and number density are specified based on an error function profile; $\text{erf}(\pi^{1/2} x_2 / \delta_{\omega,0})$ (Moser and Rogers, 1991). A constant initial temperature is chosen in each stream as $T = T_0$, the saturation temperature of the fuel; however, a temperature “spike” is added at the centerline to ignite the flame. The peak spiked temperature is denoted as $T_{F,0}$. The fuel and oxidizer species are kept completely segregated in the initial profiles through the addition of a thin layer of product species to prevent an overly fast initial reaction and to allow diffusional mixing of reactants. For all cases, the evaporated vapor mass fraction, Y_V , is initially zero everywhere. For “forced” simulations, perturbations are added to the velocity field in order to excite the growth of spanwise disturbances (see below). This results in as many as four primary vortex pairing events during a simulation, thereby allowing a more natural development of the mixing layer as compared to early times when the initial conditions are expected to have a stronger influence on the flow dynamics.

3. Numerical approach

The numerical solution procedure uses a fourth order explicit Runge–Kutta temporal integration for all time derivatives. Spatial derivatives are discretized using an explicit eighth-order

accurate central finite-difference scheme in the streamwise direction (x_1), and by a fourth order accurate tridiagonal compact finite difference in the cross stream direction (x_2) (Kennedy and Carpenter, 1994). The computational grid is uniformly spaced with constant $\Delta x_1 = \Delta x_2$. A fourth order Lagrange interpolation procedure is employed to obtain gas phase variable values at droplet locations as the droplets, in general, do not reside at grid point locations. The streamwise direction employs periodic boundary conditions, whereas adiabatic slip wall conditions are maintained for the x_2 domain boundaries. The choice of employing the slip wall boundary condition both eliminates the treatment of droplets entering and exiting the domain, and simplifies the confirmation of mass and energy conservation used for code validation. Droplets interacting with the walls are assumed to undergo an elastic collision. Although this assumption is overly simplistic for real droplets the walls are away from the primary flow regions of interest where little or no evaporation is occurring, and the effects of the assumption are deemed negligible to the results of the study.

The domain chosen for all the simulations has $L_1 = 8\lambda_1 = 58.32\delta_{\omega,0}$ and $L_2 = 1.125L_1$, where λ_1 is the smallest forcing wavelength in the x_1 direction. Sinusoidal velocity perturbations are superimposed on the base flow profile having wavelengths $L_1, L_1/2, L_1/4$ and $L_1/8$. The disturbances are generated as a spanwise vorticity distribution of the form $\omega_3 = -\sum_{m=1}^4 f(x_2) | \times A_m \sin(2\pi x_1 / (2^m \lambda_1)) |$, where the cross stream weighting is given by $f(x_2) = \exp(-\pi x_2^2 / \delta_{\omega,0}^2)$, and the relative amplitudes of the harmonics are $A_1 = 1, A_2 = 0.5, \text{ and } A_3 = A_4 = 0.35$. The appropriate Poisson equation is then solved to give the corresponding velocity disturbance distribution. The non-dimensional forcing amplitude (F_{2D}^*) is characterized by the spanwise circulation of the disturbance relative to the base flow circulation ($\lambda_1 \Delta U_0$). The imposed disturbances instigate the development of eight initial vortices together with four pairing events prior to the non-physical intervention of the domain boundaries.

The code is parallelized in both directions using the Message Passing Interface communication routines. The Courant number, C , for the single phase simulation is $C = 0.5$, whereas two-phase simulations employ $C = 0.25$ in order to ensure that the transient vaporization is well resolved temporally.

3.1. Properties and non-dimensional parameters

Table 1 presents the properties of each of the species under consideration; fuel, oxidizer, product, evaporated vapor, as well as the liquid species comprising the dispersed phase. The fuel gas and the droplets have the same properties for both non-reacting and fuel droplets. The above species properties are chosen to model a typical air-hydrocarbon diffusion flame. The oxidizer species has properties corresponding to those of air, the fuel species corresponds to decane, and the product species properties are determined from mass and energy balances based on the reaction $Fuel + rOxidizer \rightarrow (1 + r)Products$. All species are assumed to be calorically perfect and to have the same constant diffusivity Γ .

Several non-dimensional parameters are introduced in the formulation. The flow Reynolds number is given as $Re_0 = \rho \Delta U_0 \delta_{\omega,0} / \mu$. The initial droplet distribution is monodisperse with the uniform size specified by the initial Stokes number $St_0 = \tau_{d,0} \Delta U_0 / \delta_{\omega,0}$. Only the lower stream (fuel gas) is loaded with droplets. For a constant density stream with uniform mass droplets the mass loading is defined as:

Table 1
Property values of the species used in all simulations

Property	Value
W_O	28.97 kg (kg mol) ⁻¹
W_F	142.0 kg (kg mol) ⁻¹
W_P^*	57.574 kg (kg mol) ⁻¹
W_V	142.0 kg (kg mol) ⁻¹
$C_{p,O}$	1043.8 J kg ⁻¹ K ⁻¹
$C_{p,F}$	2251.5 J kg ⁻¹ K ⁻¹
$C_{p,P}$	1947.7 J kg ⁻¹ K ⁻¹
$C_{p,V}$	2394.5 J kg ⁻¹ K ⁻¹
C_L	2520.5 J kg ⁻¹ K ⁻¹
ρ_L	642.0 kg m ⁻³
$T_{B,L}$	447.7 K
h_V^0	3.36 × 10 ⁵ J K ⁻¹

All species have equal thermal conductivities and mass diffusivities with $Pr = Sc = 0.697$ ($W_p = 40.412$ kg (kg mol)⁻¹ for Case 9).

$$ML_0 = \frac{N_d m_d}{\rho L_1 L_2 L'_3 / 2}, \quad (20)$$

where N_d is the number of droplets in the stream.

A reference length in the x_3 direction must be specified to define a meaningful mass loading for a 2D flow since the droplets are spherical. Following Miller (2001) we assume that the droplets are initially distributed at the “nodes” of a hypothetical Cartesian grid in the 2D plane, in which case the corresponding homogeneous 3D distribution would have the same droplet separation in the third direction. The spanwise length scale L'_3 is defined to be this hypothetical separation distance, which is determined by equating the assumed Cartesian particle grid area to the total area of the laden stream:

$$N_d L_3'^2 = \frac{L_1 L_2}{2}. \quad (21)$$

Non-dimensional parameters also specify the chemical reaction. The Zeldovich number parameterizes the reaction activation energy: $Ze = E^0 / (R^0 T_0)$, and the heat release parameter Ce specifies the heat of reaction ΔH^0 : $Ce = -\Delta H^0 / (C_{p,F} T_0)$. With the above notation, the adiabatic flame temperature (T_F) is approximated by $T_F = T_0(1 + Ce)$, where T_0 is the initial temperature of both streams in the mixing layer. Furthermore, the temperature dependent Damkohler number (Da) is defined as the ratio of the characteristic time scale of the flow to the characteristic reaction time scale: $Da(T) = K_R(T) \delta_{\omega,0} / \Delta U_0$.

4. Results

Table 2 summarizes the simulations conducted for the present study and provides all simulation parameters. Cases 0–2 illustrate the effect of varying the mass loading ratio in the range of $0 \leq ML_0 \leq 0.5$. Case 3 utilizes a very small forcing amplitude ($F_{2D}^* = 0.001$) to study possible

Table 2

Initialization parameters: All cases have 512×576 grid points and $M_c = 0.35$, $Re_0 = 450$, $Da(T_F) = 10$, $T_{F,0} = 935$ K, $P_0 = 1$ atm, $Ce = 3.0$, and $r = 1$ (except Case 9)

Case	N_p	ML_0	St_0	F_{2D}^*	Note
0	2.11×10^5	0.5	2.0	0.1	–
1	0	–	–	0.1	–
2	1.33×10^5	0.25	2.0	0.1	–
3	2.11×10^5	0.5	2.0	0.001	–
4	1.06×10^6	0.25	0.25	0.1	–
5	0.22×10^5	0.25	12.0	0.1	–
6	2.11×10^5	0.5	2.0	0.1	Non-reacting droplets
7	2.11×10^5	0.5	2.0	0.1	Non-reacting carrier gas
8	1.89×10^5	0.5	2.0	0.1	Carrier gas = O ₂
9	2.11×10^5	0.5	2.0	0.1	$r = 4$

Two-phase simulations are initialized with zero slip velocity ($v_i = u_i$) and zero slip temperature ($T_p = T$). Case 6 has a non-reacting dispersed phase, whereas Case 7 has a non-reacting carrier gas with a reacting dispersed phase. Case 8 replaces the carrier gas fuel with oxidizer.

effects due to forcing (the mixing layer did not “roll-up” with $F_{2D}^* = 0$). The effects of the initial Stokes number are demonstrated by Cases 4 and 5, as well as by Case 0 in the range $0.25 \leq St_0 \leq 12$. The extent of the relative contribution of the evaporating droplets and the carrier fuel gas to the combustion is explained by comparing the results from simulations Case 6 (non-reacting droplets in carrier fuel gas) and Case 7 (reacting fuel droplets in non-reacting carrier fuel gas) to those of Case 0 (reacting fuel droplets in reacting carrier fuel). Case 8 replaces the carrier gas in Stream 2 with the oxidizer gas and thus investigates the combustion of only the fuel droplets (note that for this simulation the initial gas phase mixing layer has zero density stratification). Finally, the effect of increasing the reaction stoichiometric coefficient is explained by Case 9 having $r = 4$. We note here that the assumption of cluster burning made in the introduction may not be as reasonable for Cases 7 and 8 in that these flames may show more propensity for enveloping flames to occur around individual droplets. However, no such numerical approach exists for accounting for this type of flame and the results of these simulations should therefore be considered with some degree of caution. Further research is required in this area before the extent of impact of the cluster burning assumption can be more properly quantified.

The remaining initialization parameters are fixed for all the simulations. The uniform temperature in both streams is $T_0 = 447.7$ K; i.e. the normal fuel boiling temperature. The spiked ignition temperature is chosen to be $T_{F,0} = 935$ K. The convective Mach number is $M_c = 0.35$ and the flow Reynolds number is $Re_0 = 450$. The heat release parameter is $Ce = 3$ ($T_F = 1790$ K) and the Damkohler number evaluated at the adiabatic flame temperature is chosen to be $Da(T_F) = 10$. For the dispersed phase in all simulations, the droplets are initially randomly dispersed throughout the carrier stream with specified size. Also, the droplets initially have zero slip velocity and zero slip temperature. The initial droplet temperature is chosen to be equal to the surrounding (saturation) temperature such that the gas and liquid phases are in equilibrium. All simulations are conducted until a non-dimensional time $t^* = t \Delta U_0 / \delta_{\omega,0} = 160$ at which point the final pairing has been nearly completed. Note that a pure saturated gas/liquid fuel stream is not meant to

mimic actual combustor conditions. This condition is chosen only in order to simplify the analysis.

4.1. Flow visualizations

A qualitative analysis of the evolution of the mixing layer and flame development is introduced in this section aided by flow visualizations. Figs. 2 and 3 present the droplet concentration and the temperature contours at times $t^* = 80$ and 160 for the simulation Case 2. Inverse shading has been

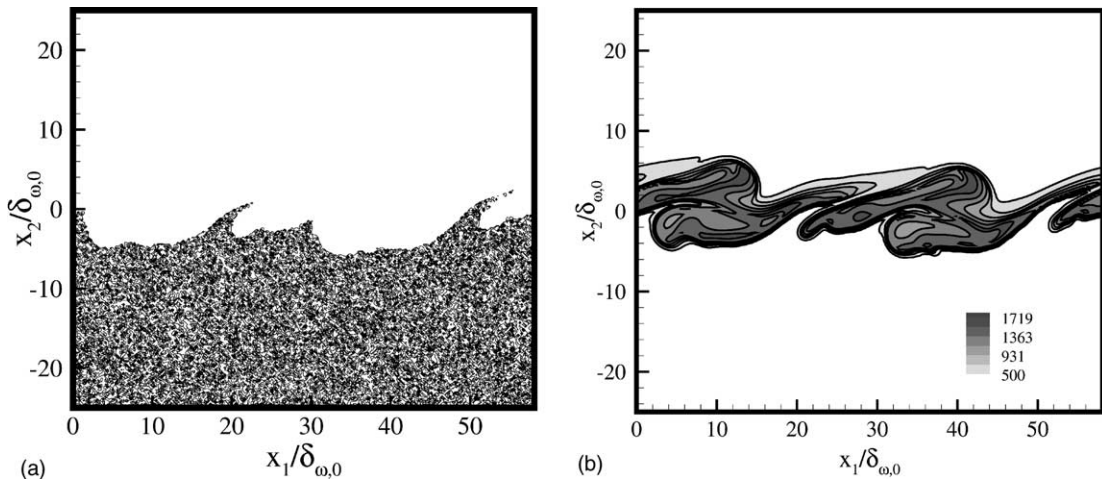


Fig. 2. Contours for simulation Case 2; (a) droplet number density at time $t^* = 80$, and (b) temperature at time $t^* = 80$.

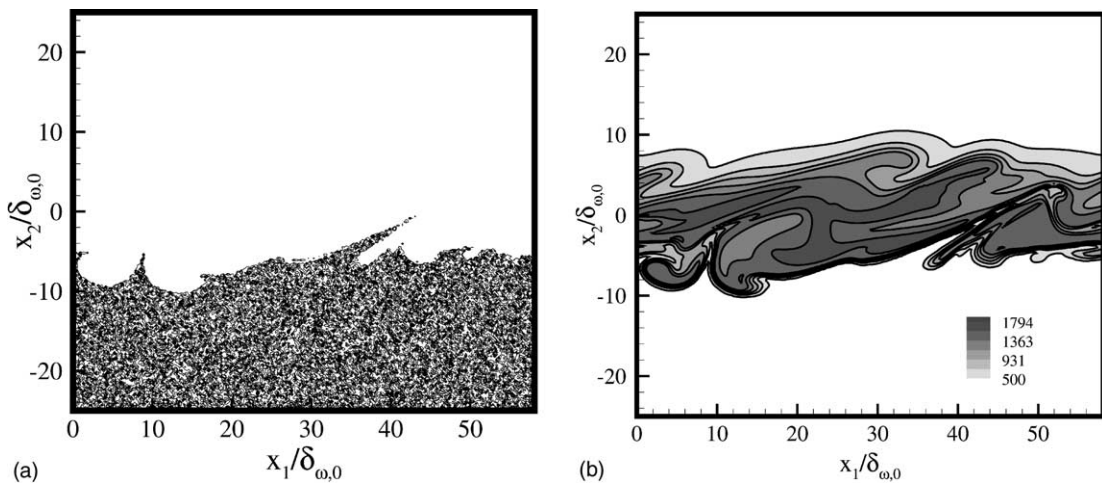


Fig. 3. Contours for simulation Case 2; (a) droplet number density at time $t^* = 160$, and (b) temperature at time $t^* = 160$.

used to highlight larger temperatures with darker shading. For all gray scale contour plots, the maximum labeled contour indicates the maximum domain value. The dispersed phase in the form of reacting fuel droplets displays two competing effects. The evaporation phase change of the fuel droplets tends to decrease the gas temperature owing to latent heat effects, whereas the evaporated fuel vapor from the droplets (in addition to the carrier fuel gas) contributes to the reaction, potentially aiding combustion in the mixing layer. Miller (2001) showed that latent heat effects from non-reacting droplets can cause local flame extinction in a similar reacting mixing layer (see also the following discussion for Case 6). However, the present reaction is sufficiently enhanced by the droplet fuel at all times such that local flame extinction is not directly apparent in the flow visualizations (Figs. 2(b) and 3(b)).

Figs. 4 and 5 provide the product mass fraction and the evaporated vapor mass fraction contours at times $t^* = 80$ and 160 for the simulation Case 2. At $t^* = 80$ the second set of pairings is occurring. At this time, the preferential concentration of the droplets into the high strain braids of the mixing layer is evident from the number density contours (Fig. 2(a)). However, the maximum temperatures are observed at places with maximum evaporated vapor mass fraction (see Figs. 2(b) and 5, or Figs. 3(b) and 5(b)) since the evaporated fuel vapor increases the total amount of fuel mass available and hence aids the combustion. This is verified from the product mass fraction contours in Fig. 4(a). At the final simulation time of $t^* = 160$ the final pairing is nearly complete. Any droplets unable to escape the burning vortices are completely evaporated as depicted by the number density and temperature contours (Figs. 3(a) and (b)).

A comparison of the temperature contours (Fig. 3(b)) and the product mass fraction contours (Fig. 4(b)) for the final time illustrates that regions of high temperature are correlated with regions of large product mass fraction. However, maximum temperatures (Fig. 3(b)) are again supported by maximum evaporated vapor fuel mass available to aid combustion (Fig. 5(b)) as discussed earlier with a maximum of $T_{MAX} = 1794$ K. In these regions along the periphery of the flame fresh droplets continue to evaporate providing additional fuel to feed the combustion.

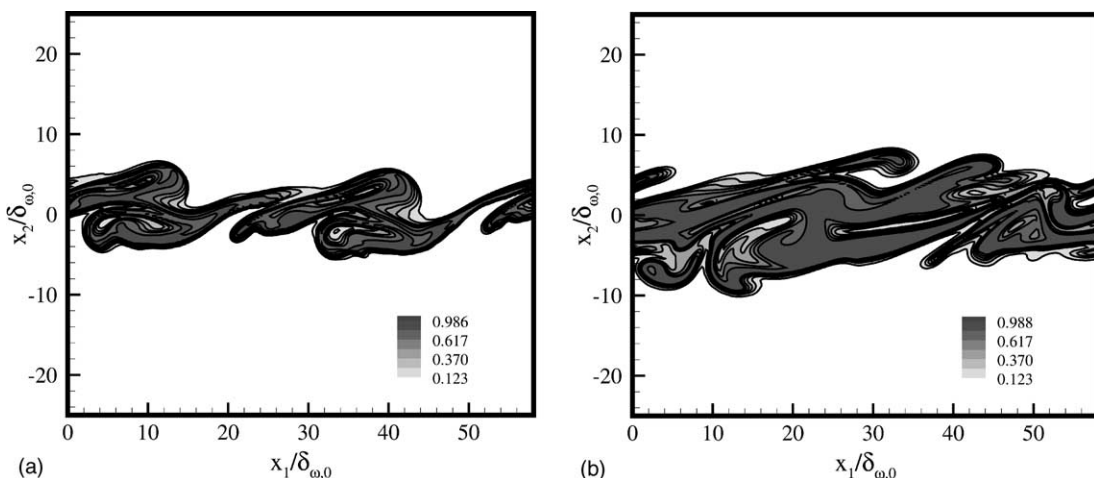


Fig. 4. Contours of the product mass fraction for simulation Case 2 at times (a) $t^* = 80$, and (b) $t^* = 160$.

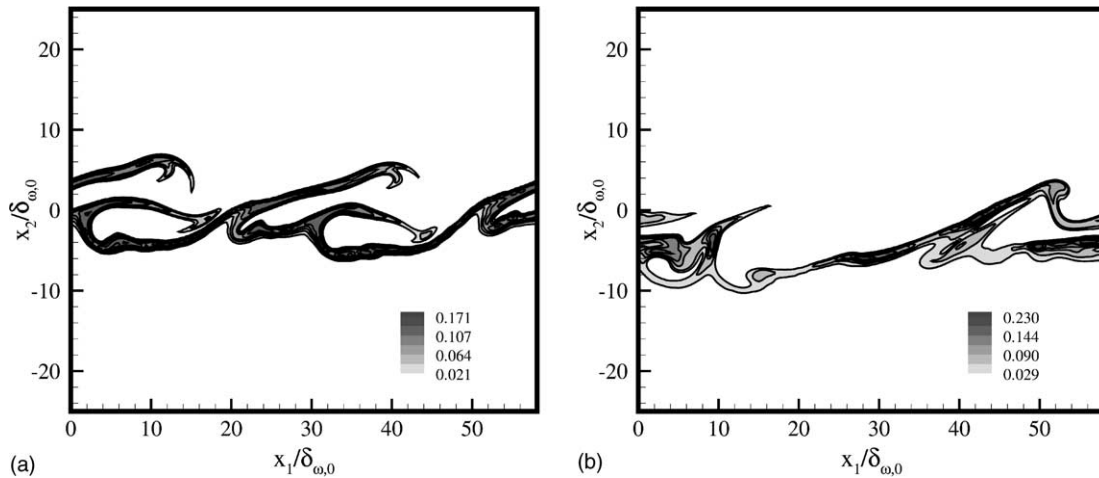


Fig. 5. Contours of the evaporated vapor mass fraction for simulation Case 2 at times (a) $t^* = 80$, and (b) $t^* = 160$.

4.2. Effects of fuel and reaction stoichiometric coefficient

The effects of the fuel composition on the reacting mixing layer are analyzed for five flow configurations: (1) fuel droplets in carrier fuel (base case), (2) single phase flame, (3) non-reacting droplets in carrier fuel, (4) reacting fuel droplets in non-reacting carrier fuel gas, and (5) reacting fuel droplets in carrier oxidizer. The effect of varying the reaction stoichiometric coefficient is also considered by Case 9 with $r = 4$.

The extent of local extinction is quantified with $\alpha_F(\chi)$, “the extinction factor”, (Miller, 2001) which is bounded by $0 \leq \alpha_F(\chi) \leq 1$ and signifies the relative fraction of the domain with “pre-mixed” reactants having a non-dimensional temperature greater than χ , where $\chi = (T - T_0)/(T_F - T_0)$ is the relative gas temperature between the ambient and the adiabatic flame temperature:

$$\alpha_F(\chi) = \frac{\int_{-L_2/2}^{+L_2/2} \int_0^{L_1} H(\chi(\vec{x}) - \chi) H(Y_O Y_F(\vec{x}) - 5.0 \times 10^{-5}) dx_1 dx_2}{\int_{-L_2/2}^{+L_2/2} \int_0^{L_1} H(Y_O Y_F(\vec{x}) - 5.0 \times 10^{-5}) dx_1 dx_2}, \quad (22)$$

where H is the Heaviside function and the product $Y_O Y_F$ indicates the potential for chemical reactions to occur (see Eqs. (6)–(8)).

Fig. 6 presents the temporal development of the maximum temperature and the extinction factor $\alpha_F(\chi = 0.1)$ for the flow configurations described above. Here, $\chi = 0.1$, which corresponds to a temperature of $T = 582$ K, is chosen to estimate the proportions of reacting and non-reacting fluid regions for the following analysis. The value $\chi = 0.1$ was chosen following Miller (2001) based on the reaction rate resulting at this temperature for the chosen Zeldovich and Damkohler numbers as being sufficient to produce robust conversion rates.

At early times, both the peak temperature and the extinction factor are observed to initially decrease for all cases (Fig. 6(a) and (b)). This ignition delay, and a corresponding decrease in the initial peak temperature, can be attributed to the initially segregated fuel and oxidizer requiring sufficient time for diffusional mixing prior to the commencement of combustion. Once combustion

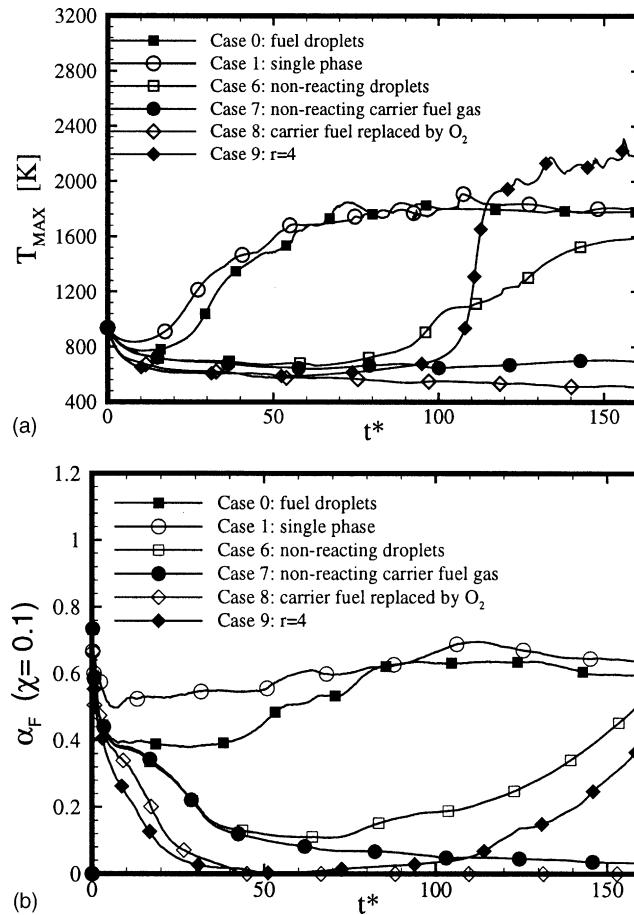


Fig. 6. Temporal development of (a) the maximum temperature, and (b) the extinction factor.

begins, the reaction rate for the fuel droplets (Case 0) and for the single phase flow (Case 1) configurations is higher due to a larger presence of mixed fuel and oxidizer, and a faster increase in the peak temperature is observed for these cases (see Fig. 6(a)). The single phase case has the highest reaction rate at early times as it is unimpeded by droplet latent heat effects, which is also supported by a high extinction factor at all times. Case 0 closely follows the single phase case after the ignition delay due to the presence of the fuel droplets which also contribute to the reaction. Hence a faster increase in the peak temperature is observed as opposed to the non-reacting droplets case (Case 6) which has a comparatively much larger ignition delay ($t^* = 60$). This delay in ignition for Case 6 allows for an eventually enhanced diffusional mixing of the reactants, followed by a relatively robust combustion. A final time peak temperature of $T_{MAX} \sim 1790$ K is observed for Cases 0 and 1.

Case 9, with a reaction stoichiometric coefficient of $r = 4$, has a much longer ignition delay ($t^* \sim 70$). The delay in ignition can be attributed to a longer time required for the mixing of reactants in order for a strong combustion to take place due to the larger amount of oxidizer re-

quired to react with the fuel (4:1). However, due to increased concentration of the mixed reactants caused by the ignition delay, once begun, combustion proceeds vigorously (Fig. 6(a)) and a peak temperature of $T_{MAX} = 2162$ K is observed for Case 9. As indicated by Fig. 6(b), Case 9 is characterized by a very localized flame with relatively large portions of mixed reactants remaining quenched for the duration of the simulation. A corresponding rapid growth of the product thickness is also observed due to the ignition delay for Case 9 (see Fig. 7(b)).

Case 7 employs a non-reacting carrier fuel gas configuration, whereas Case 8 replaces the carrier fuel gas with oxidizer. In both cases, the droplets are the only source of fuel for combustion in the flow. Two primary differences distinguish Cases 7 and 8. Firstly, for Case 7 the density stratification of the base simulations is retained, whereas Case 8 has no density stratification in the initial gas phase. Secondly, the carrier fuel for Case 7 (though non-reacting) retains the thermodynamic saturation of droplets in the free stream, thereby impeding droplet evaporation. As

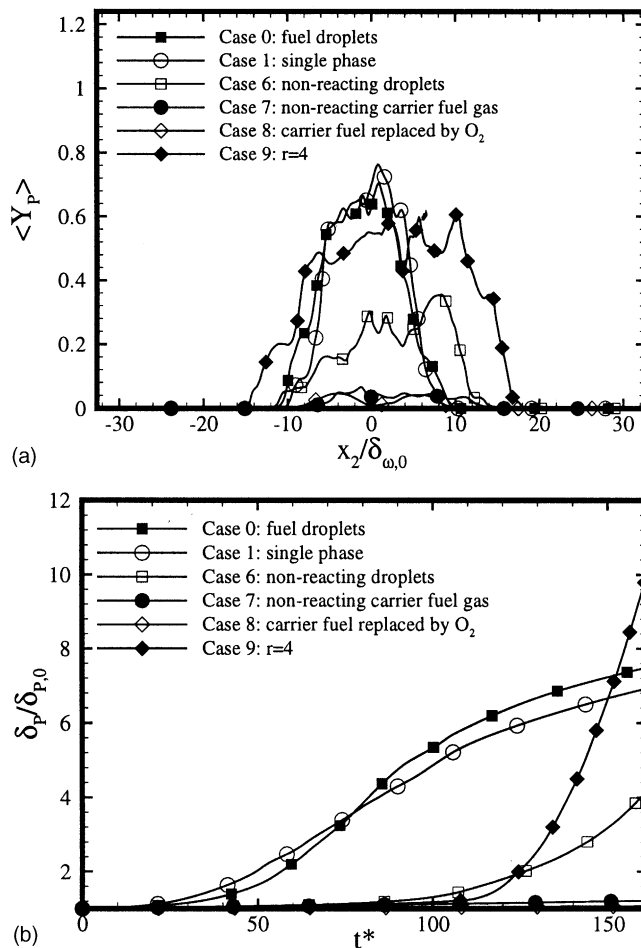


Fig. 7. (a) x_2 profile of the average product mass fraction, and (b) temporal evolution of the normalized product thickness.

indicated by Fig. 6(a) and (b), both Cases 7 and 8 fail to achieve robust combustion with very low peak temperatures due to insufficient fuel mass available for combustion, as well as by the dilution of reactants by the non-reacting carrier fuel (Case 7). This feature is supported by temporally decreasing extinction factors (Fig. 6(b)); suggesting the primary contribution of the carrier fuel gas on efficient combustion for the conditions of the present study. However, the final time peak temperature of Case 7 (690 K) is higher than that for Case 8 (506 K) as observed from Fig. 6(a). This feature is attributed to a relatively large evaporation of the decane droplets for Case 8 owing to saturation effects for Case 7; the carrier fuel gas being decane.

Fig. 7 presents the final time x_2 profiles for the average product mass fraction and the temporal development of the normalized product thickness for all cases. The maximum product mass fraction ($\langle Y_p \rangle \approx 0.76$) is observed for the single phase case at the center of the reacting mixing layer (Case 1; Fig. 7(a)). This is attributed to the absence of the evaporating droplets and their associated latent heat effects as discussed earlier. The fuel droplets case (Case 0) and the $r = 4$ case (Case 9) both display relatively large product mass fractions due to the presence of fuel droplets contributing to combustion. However, a very low product mass fraction is observed for Case 7 (non-reacting carrier fuel gas) owing to the dilution of the reactants by the non-reacting carrier fuel gas discussed above. The broad x_2 range of values of the product mass fraction for the $r = 4$ case (Case 9) signifies a more intense vortical rollup as compared to other cases allowed by the delay in ignition. The product thickness remains low at early times for this flow due to the aforementioned delay in ignition (see Fig. 7(b)). This ignition delay aids the pre-mixing of reactants and hence a rapid escalation of the product thickness is observed for later times (Fig. 7(b)).

Fig. 8 presents the final time ($t^* = 160$) temperature contours for the fuel droplet (Case 0) and the non-reacting droplet (Case 6) simulations. Local extinction is clearly evident for Case 6 for which the droplets contribute latent heat effects, but not added fuel. Even at the final simulation time, a well defined layer of extinguished fluid resides between the two primary vortices (Fig. 8(b)) since the reaction rate is too slow to overcome the effects of the cooling in the braids of the mixing layer caused by the preferentially concentrated droplets. However, for Case 0, the reaction is

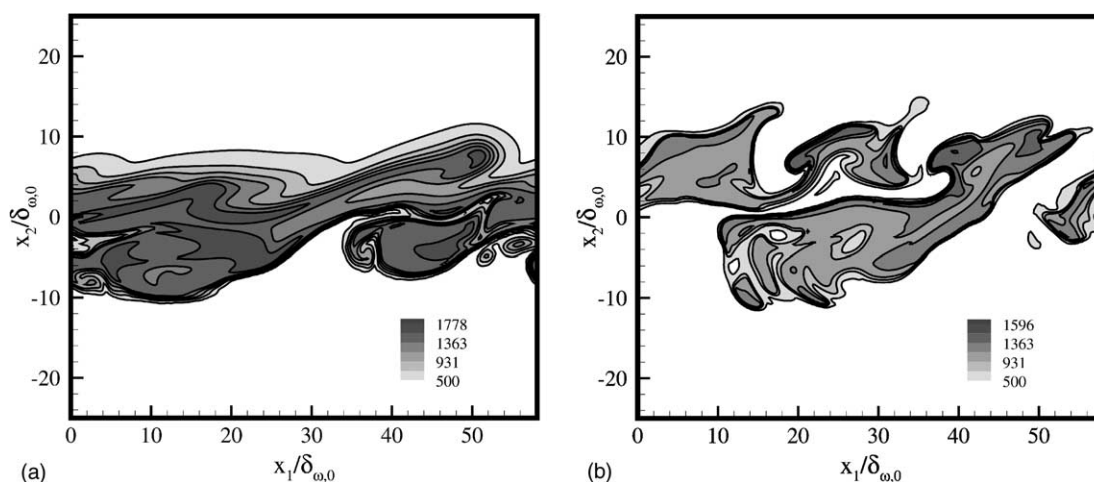


Fig. 8. Temperature contours at $t^* = 160$ for (a) Case 0 (fuel droplets), and (b) Case 6 (non-reacting droplets).

sufficiently strong to prevent local flame extinction in the braids of the mixing layer due to the presence of the fuel droplets.

4.3. Effects of mass loading

The effect of the mass loading ratio is analyzed for three different configurations: Case 0 ($ML_0 = 0.5$), Case 1 (single phase flame; $ML_0 = 0$), and Case 2 ($ML_0 = 0.25$). Fig. 9 presents the temporal development of the maximum temperature and the extinction factor for the above configurations. It is observed that, until $t^* \approx 50$, both the maximum temperature and the extinction factor decrease with the addition of more droplets due to their finite thermal inertia and associated latent heat effects. However, the final time peak temperatures and extinction factors are comparable for the considered configurations. Miller (2001) studied the effects of non-reacting droplet loading on a reacting mixing layer and observed large differences in the trend of the peak temperature temporal development. These differences were attributed to the droplet thermal

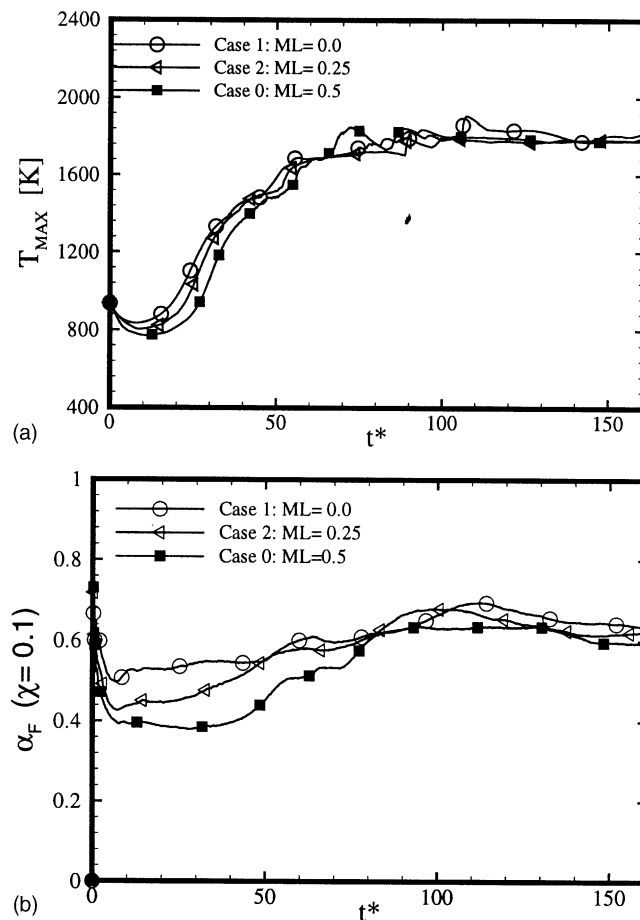


Fig. 9. Temporal development of (a) the maximum temperature, and (b) the extinction factor.

inertia and the corresponding tendency of the droplets to cool the surrounding fluid. However, in the present results, the presence of a reacting dispersed phase tends to decrease the difference in the peak temperature temporal development for various mass loadings due to the competing influence of added fuel mass available for combustion.

4.4. Effects of the Stokes number

This section investigates the effects of the initial droplet size, quantified by the initial Stokes number, St_0 . All earlier discussed configurations employ a moderate Stokes number of 2.0. Here, the effects of the Stokes number are analyzed for small ($St_0 = 0.25$), moderate ($St_0 = 2.0$), and large ($St_0 = 12.0$) droplets for a fixed mass loading of 0.25. The temporal development of the peak temperature and the extinction factor are presented in Fig. 10. The changes in the initial Stokes number do not significantly affect the growth rate of the mixing layer as observed by Fig. 10. These results are in agreement with earlier findings for non-reacting particles and droplets (Miller,

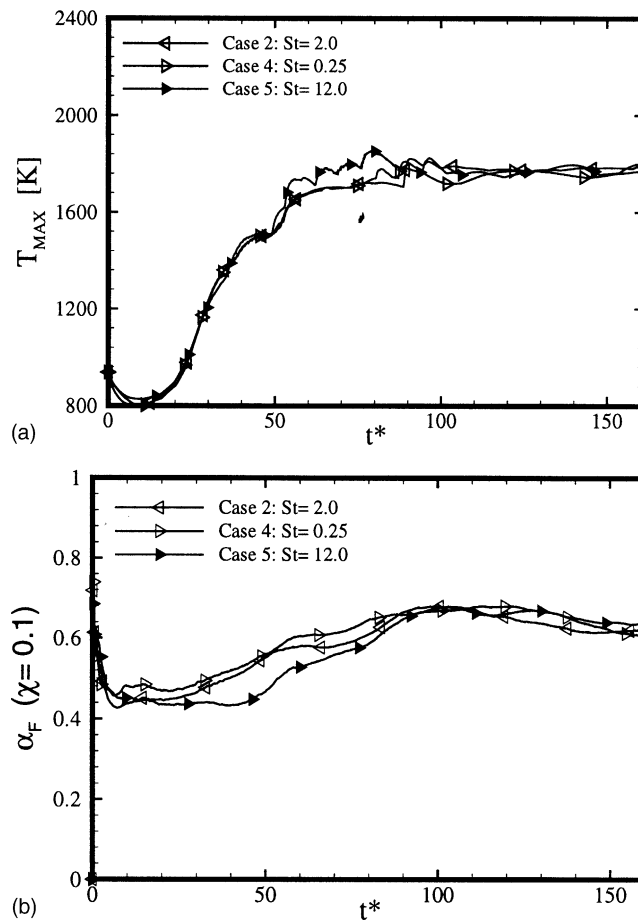


Fig. 10. Temporal development of (a) the maximum temperature, and (b) the extinction factor.

2001; Miller and Bellan, 1999). However, at intermediate times, for large droplets ($St_0 = 12.0$), the peak temperature is observed to be relatively higher (see Fig. 10(a)) as compared to the small and moderate Stokes number cases. This feature can be attributed to the relatively large droplet size, since large droplets do not closely follow fluid motions and hence are less entrained in the mixing layer. The reduced entrainment allows local portions of the flame to burn with relatively low droplet (latent heat) content, achieving locally high temperatures. However, the droplets that are present in the flame initially have a relatively long lifetime due to their increased size. These relatively long-lived droplets extend the duration over which their latent heat affects the flame structure of the braid regions; thereby resulting in lower extinction factor for both early and intermediate times.

4.5. Effects of forcing

The effects of the forcing amplitude on the mixing layer growth and configuration are studied for two forcing amplitudes ($F_{amp} = 0.1$ and $F_{amp} = 0.001$) in order to investigate the extent to which the results may be affected by the forcing. The $F_{amp} = 0.001$ case is compared with the $F_{amp} = 0.1$ at a time when it develops the same final time momentum thickness ($t^* = 340$). An additional case having $F_{amp} = 0$ was also conducted, but did not result in vortical rollup (not shown). Fig. 11 displays the temporal development of the peak temperature and the extinction factor for both cases. Employing a higher forcing amplitude in the flow configuration is observed to hasten the growth of the mixing layer. However, the qualitative mixing layer statistics are preserved (Fig. 11) and the final time peak temperatures as well as the extinction factor values are observed to be nearly equal. This suggests the validity of using relatively high forcing amplitudes for the present mixing layer configuration. An examination of other flow parameters supports this observation (not shown). However, some quantitative statistical differences are observed from Fig. 12, which elucidates the cross stream statistics of the average product fraction and the average gas temperature. Higher forcing amplitude is observed to result in a higher average product fraction (Fig. 12(a)) and a higher average gas temperature (Fig. 12(b)). An increased convolution of the flame surface in the presence of forcing enhances “turbulent” mixing and combustion efficiency resulting in the observed trends.

4.6. Probability density function analysis

The statistical distribution of the mixture fraction is considered to provide a quantitative analysis of the mixing. Fig. 13(a) depicts the probability density function (PDF) of the mixture fraction as a function of the cross stream direction x_2 , and Fig. 13(b) provides the PDF of the mixture fraction at the center of the mixing layer ($x_2 = 0$) at the final simulation time ($t^* = 160$) for Case 0. The mixture fraction, defined as $\phi = (1 + Y_F - Y_O)/2$, Miller and Bellan (1998) is a conserved scalar variable independent of the reaction rate (for non-heat releasing chemistry) and of the evaporation source term. As indicated by Fig. 13(a), the probability of finding mixed fluid in the reacting mixing layer varies in the range $-10 \leq x_2 \leq +10$. The probability of finding pure reactant species at the center of the mixing layer is zero as indicated by Fig. 13(b). The PDFs presented in Fig. 13 are consistent with the findings of Miller et al. (1994) for “pre-transitional” flows. They illustrated the cross stream variation of the mixture fraction PDF for pre-, mid-, and

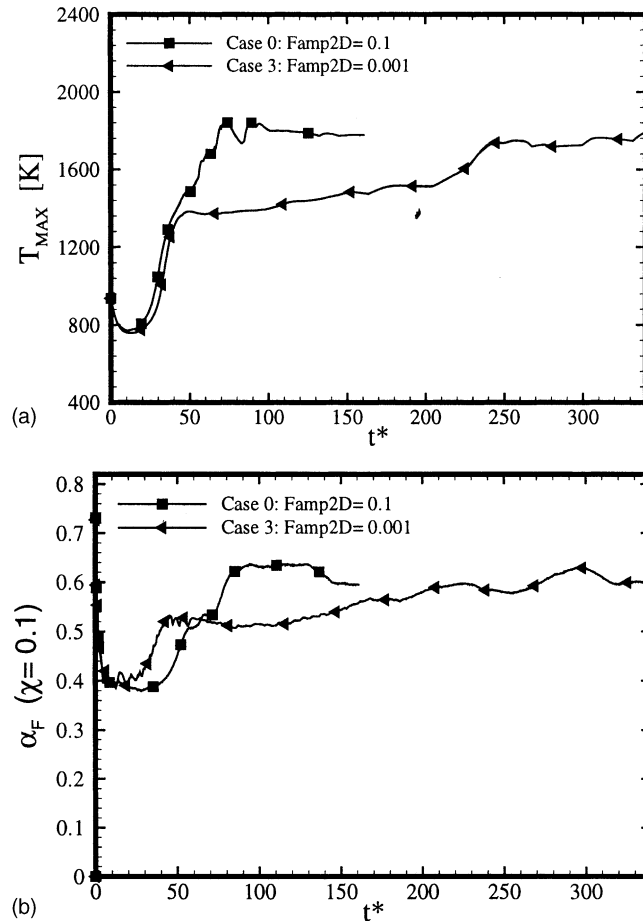


Fig. 11. Temporal development of (a) the maximum temperature, and (b) the extinction factor.

post-transitional flows for a three-dimensional reacting mixing layer and found that turbulent flames are characterized by largely enhanced probabilities of mixed fluid regions. However, the present results are for 2D mixing layers which cannot undergo true transition to turbulence and therefore do not produce large probabilities associated with truly turbulent flows.

Fig. 14 presents the mixture fraction PDFs for the $r = 4$ (Case 9) configuration. In comparison with the PDF for Case 0 (see Fig. 13), it is clearly evident that the range of probability of finding mixed fluid is approximately doubled varying in the range $-20 \leq x_2 \leq +20$ (Fig. 14). This signifies a more intense vortical rollup and hence relatively better mixing based on the delayed ignition described previously. The centerline PDF in Fig. 14(b) confirms this increased mixing efficiency due to its more “compact” distribution around the $\phi = 0.5$ perfectly mixed value in comparison with Fig. 13(b). However, in spite of the fact that the probability of finding pure oxidizer ($\phi = 0$) is zero at the center of the mixing layer, the probability of finding pure fuel vapor ($\phi = 1$) is significant (see Fig. 14(b)). This indicates that the relatively intense vortical rollup continues to entrain fuel into the mixing layer, with insufficient oxidizer for complete combustion to occur.

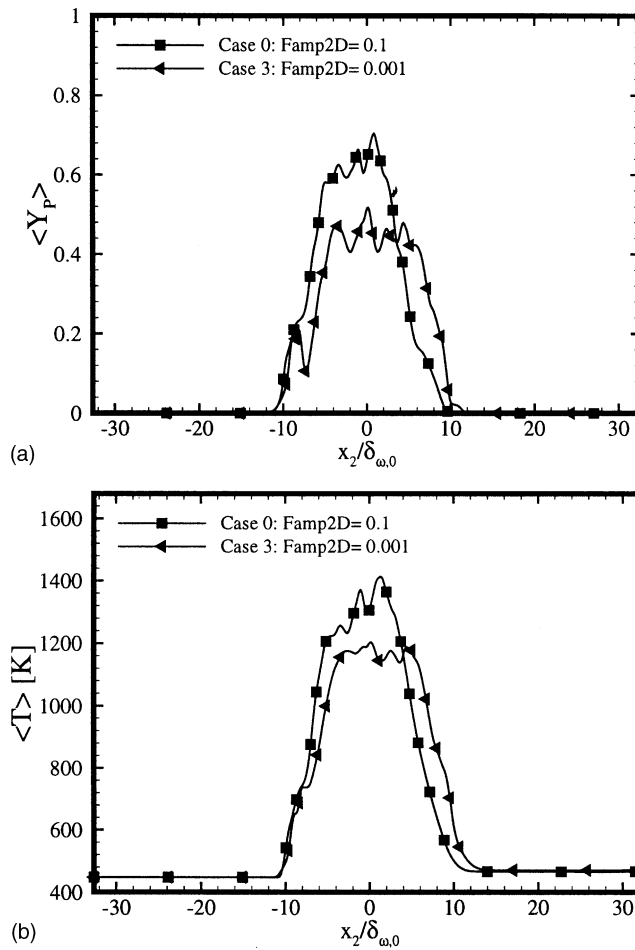


Fig. 12. Cross stream profile of (a) the average product fraction, and (b) the average gas temperature at $t^* = 160$.

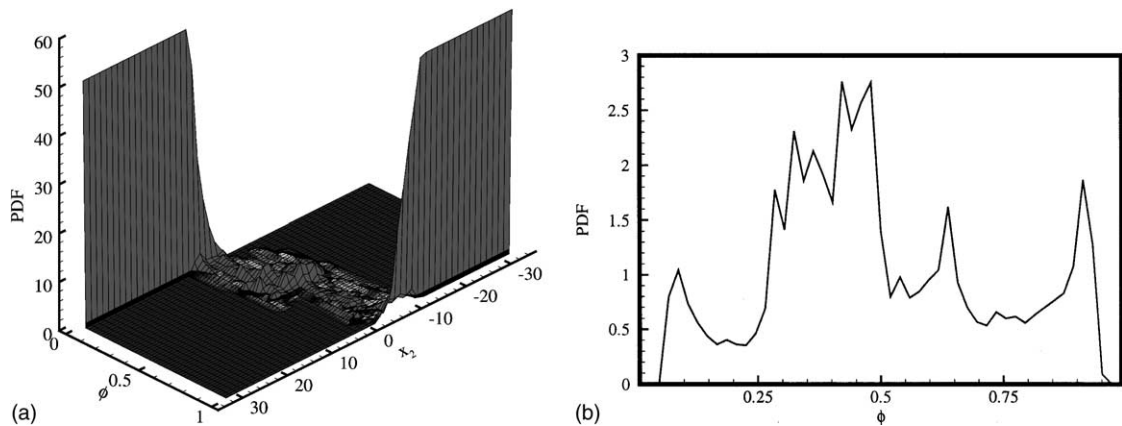


Fig. 13. PDF of the mixture fraction for the simulation Case 0 at $t^* = 160$; (a) PDF vs. x_2 , and (b) PDF at the center of the mixing layer ($x_2 = 0$).

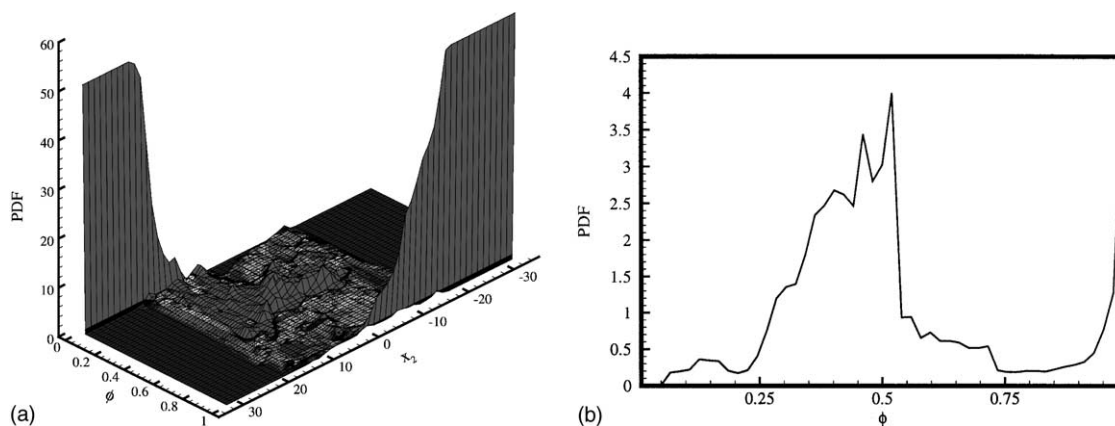


Fig. 14. PDF of the mixture fraction for the simulation Case 9 at $t^* = 160$; (a) PDF vs. x_2 , and (b) PDF at the center of the mixing layer ($x_2 = 0$).

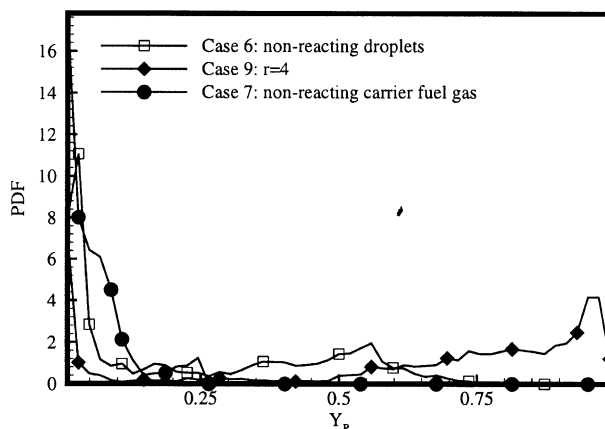


Fig. 15. PDF of the product mass fraction at the center of the mixing layer ($x_2 = 0$) at $t^* = 160$.

The PDFs of the product mass fraction for Cases 6, 9 and 7 are displayed in Fig. 15. As observed earlier, Case 7, employing a non-reacting carrier fuel gas, fails to achieve combustion signifying the primary role of the carrier fuel in combustion. As indicated by Fig. 15, the probability of finding zero product mass fraction is maximum with zero probability of finding $Y_p \geq 0.25$. Case 6, which employs a non-reacting droplet phase displays a relatively higher probability of finding product mass at the center of the mixing layer. However, the probability of finding $Y_p \geq 0.75$ is zero for Case 6. In contrast, the $r = 4$ case displays relatively high probability of finding product mass, with a significant probability of finding pure product ($Y_p = 1$).

5. Conclusions

Numerical simulations of fuel droplet laden reacting mixing layer diffusion flames were conducted considering an irreversible and exothermic reaction of the form $Fuel + rOxidizer \rightarrow$

$(1 + r)$ Products. The droplets were assumed to be spherical and to obey a modified Stokes drag law. Both the carrier gas fuel and the liquid droplet properties were the same corresponding to those of decane, while the carrier oxidizer utilized the properties of air. The droplet evaporated vapor also contributed to the reaction aiding in combustion. The simulation parameters chosen addressed the effects of fuel composition, the reaction stoichiometric coefficient, the mass loading ratio, the initial droplet Stokes number, and the flow forcing amplitude.

The evolution and growth of the two-phase mixing layer was observed to be essentially independent of the mass loading ratio and the droplet initial Stokes number. A quantitative analysis was conducted to estimate the extent of the relative contribution of different forms of fuel to combustion. The presence of a reacting dispersed phase was observed to reduce local flame extinction as opposed to a non-reacting dispersed phase displaying highly evident local flame extinction. The mixing layer configuration employing a higher reaction stoichiometric coefficient was observed to display a much longer delay in ignition. However, due to this delay, better diffusional mixing of the reactants was allowed and hence a more robust and organized combustion occurred. Employing a high flow forcing amplitude was observed to accelerate the growth of the mixing layer. Although there were some quantitative differences in the mixing layer statistics, the qualitative statistics were preserved in comparison to a test case having negligible forcing amplitude.

Acknowledgement

This research was supported by the National Science Foundation through the Faculty Early Career Development (CAREER) Program; grant CTS-9983762.

References

- Boivin, M., Simonin, O., Squires, K.D., 1998. Direct numerical simulation of turbulence modulation by particles in isotropic turbulence. *J. Fluid Mech.* 375, 235–263.
- Brown, G.L., Roshko, A., 1974. On density effects and large scale structure in turbulent mixing layers. *J. Fluid Mech.* 64, 775–816.
- Chein, R., Chung, J.N., 1987. Effects of vortex pairing on particle dispersion in turbulent shear flows. *Int. J. Multiphase Flow* 13, 785–802.
- Eaton, J.K., Fessler, J.R., 1994. Preferential concentration of particles by turbulence. *Int. J. Multiphase Flow* 20, 169–209.
- Elghobashi, S., 1994. On predicting particle-laden turbulent flows. *Appl. Sci. Res.* 52, 309–329.
- Elghobashi, S., Truesdell, G.C., 1993. On the two-way interaction between homogeneous turbulence and dispersed solid particles. I: Turbulence modification. *Phys. Fluids A* 5, 1790–1801.
- Huang, L.S., Ho, C.M., 1990. Small-scale transition in a plane mixing layer. *J. Fluid Mech.* 210, 475–500.
- Karpetis, A.N., Gomez, A., 2000. An experimental study of well-defined turbulent nonpremixed spray flames. *Combust. Flame*, 1–23.
- Kennedy, C.A., Carpenter, M.H., 1994. Several new numerical methods for compressible shear-layer simulations. *App. Numer. Math.* 14, 397–433.
- Lazaro, B.J., Lasheras, J.C., 1989. Particle dispersion in a turbulent, plane, free shear layer. *Phys. Fluids A* 1, 1035–1044.
- Martin, J.E., Meiburg, E., 1994. The accumulation and dispersion of heavy particles in forced two-dimensional mixing layers, i. The fundamental and subharmonic cases. *Phys. Fluids* 6, 1116–1132.

- Mashayek, F., 1998a. Direct numerical simulations of evaporating droplet dispersion in forced low mach number turbulence. *Int. J. Heat Mass Transfer* 41, 2601–2617.
- Mashayek, F., 1998b. Droplet-turbulence interactions in low mach number homogeneous shear two-phase flows. *J. Fluid Mech.* 367, 163–203.
- Mashayek, F., 2000. Numerical investigation of reacting droplets in homogeneous shear turbulence. *J. Fluid Mech.* 405, 1–36.
- Maxey, M.R., Patel, B.K., Chang, E.J., Wang, L.P., 1997. Simulations of dispersed turbulent multiphase flow. *Fluid Dyn. Res.* 20, 143–156.
- Meiburg, E., Wallner, E., Pagella, A., Riaz, A., Hartel, C., Necker, F., 2000. Vorticity dynamics of dilute, two-way coupled particle laden mixing layers. *J. Fluid Mech.* 421, 185–227.
- Miller, R.S., 2001. Effects of non-reacting solid particle and liquid droplet loading on an exothermic reacting mixing layer. *Phys. Fluids*, 3303–3320.
- Miller, R.S., Bellan, J., 1998. On the validity of the assumed pdf method for modeling binary mixing/reaction of evaporated vapor in gas/liquid-droplet turbulent shear flow. In: *Proceedings of the 27th Symposium (International) on Combustion*. pp. 1065–1072.
- Miller, R.S., Bellan, J., 1999. Direct numerical simulation of a confined three-dimensional gas mixing layer with one evaporating hydrocarbon-droplet laden stream. *J. Fluid Mech.* 384, 293–338.
- Miller, R.S., Bellan, J., 2000. Direct numerical simulation and subgrid analysis of a transitional droplet laden mixing layer. *Phys. Fluids* 12, 650–671.
- Miller, R.S., Madnia, C.K., Givi, P., 1994. Structure of a turbulent reacting mixing layer. *Combust. Sci. Technol.* 99, 1–36.
- Miller, R.S., Harstad, K., Bellan, J., 1998. Evaluation of equilibrium and non-equilibrium evaporation models for many-droplet gas–liquid flow simulations. *Int. J. Multiphase Flow* 24, 1025–1055.
- Moser, R.D., Rogers, M.M., 1991. Mixing transition and the cascade to small scales in a plane mixing layer. *Phys. Fluids A* 3, 1128–1134.
- Papamoschou, D., Roshko, A., 1988. The compressible turbulent mixing layer: an experimental study. *J. Fluid Mech.* 197, 453–477.
- Smith, N.S.A., Ruetsch, G.R., Oefelein, J., Ferziger, J.H., 1998. Simulation and modeling of reacting particles in turbulent nonpremixed combustion. In: *Center of Turbulence Research Proceedings of the Summer Program*. pp. 39–60.
- Squires, K.D., Eaton, J.K., 1990. Particle response and turbulence modification in isotropic turbulence. *Phys. Fluids A* 2, 1191–1203.
- Squires, K.D., Eaton, J.K., 1991. Preferential concentration of particles by turbulence. *Phys. Fluids A* 3, 1169–1178.
- Squires, K.D., Eaton, J.K., 1994. Effect of selective modification of turbulence on two-equation models for particle-laden turbulent flows. *J. Fluids Eng.* 116, 778–784.
- Sundaram, S., Collins, L.R., 1999. A numerical study of the modulation of isotropic turbulence by suspended particles. *J. Fluid Mech.* 379, 105–143.
- Truesdell, G.C., Elghobashi, S., 1994. On the two-way interaction between homogeneous turbulence and dispersed solid particles. II: Particle dispersion. *Phys. Fluids* 6, 1405–1407.
- Wakabayashi, T., Mizutani, Y., Katsuki, M., Akamtsu, F., 1998. Observations of the structure of a spray flame in 2-d counterflow burner. *AIAA Paper* 98-0720.
- Wen, F., Kamalu, N., Chung, J.N., Crowe, C.T., 1992. Particle dispersion by vortex structures in plane mixing layers. *ASME J. Fluids Eng.* 114, 657–666.
- Winant, C.D., Browand, F.K., 1974. Vortex pairing: the mechanisms of turbulent mixing layer growth at moderate Reynolds number. *J. Fluid Mech.* 63, 237–255.